RSC Advances

PAPER

View Article Online
View Journal | View Issue

Cite this: *RSC Adv.*, 2026, **16**, 28292

Development of a green and sustainable rice husk nanosilica-based spectrophotometric probe for dual detection of Ag(I) and Fe(III) in environmental and E-waste matrices

Ahmad A. Alluhaybi,[a] Azza Attia,[b] Musa A. Said, *[c] Thamer S. Alraddadi, [c] Biprajit Sarkar, [d] Reda F. M. Elshaarawy, *[e] Ahmed Shahat [c] and Mohamed Shenashen [f]

The development of sustainable, economical sensing platforms for rapid monitoring of toxic metals is a critical priority for environmental safety. In this work, a new dual-functional BNP@RHNS nanocomposite sensor was fabricated by immobilizing Br-naphthophen ligand onto agrowaste (rice husk)-derived mesoporous nanosilica. The sensor surface maintains the amorphous nanosilica framework and successfully anchors ligands covalently or non-covalently, according to the physicochemical characterization methods used. The sensor exhibited remarkable spectrophotometric selectivity toward Ag^{+} and Fe^{3+} ions in aqueous environments with an optimized response time <40 s. The method also showed broad linear dynamic ranges of 0–0.8 ppm and 0–0.85 ppm, and low limits of detection (LOD) of 0.185 ppm and 0.247 ppm for Ag^{+} and Fe^{3+} ions under the optimized conditions (pH 6.2 & pH 3.6 at 25 °C). The sensing mechanism was meticulously detailed through experimental spectral shifts and corroborated by Density Functional Theory (DFT) calculations. The theoretical work showed that the recognition process is governed by the spontaneous formation of stable coordinate complexes located in the ligand's N_2O_2 cavity. Moreover, the sensor exhibited high interfering tolerance and was successfully applied to determining metal ions in real water matrices with satisfactory recovery rates (97.37% to 100.73%). Furthermore, this sensor was found to be effective in recovering Ag(I) from leachates of electronic waste, suggesting its broader applicability in urban mining and resource recovery. These findings suggest a promising alternative valorization strategy for rice husk biomass into high-value functional materials for advanced environmental monitoring applications.

Received 19th March 2026
Accepted 18th May 2026

DOI: 10.1039/d6ra02312f

rsc.li/rsc-advances

1 Introduction

The increasing pollution of global aquatic ecosystems by inorganic substances has become a significant environmental issue, propelled by rapid industrialization, metallurgical effluents, and insufficient wastewater management practices.[1–3] In contrast to organic pollutants, heavy metal ions are non-biodegradable, resulting in their long-term presence in the environment and subsequent bioaccumulation within the food web. Therefore, there is an earnest requirement for developing effective, dual-functional platforms that can facilitate both detection and remediation to ensure water security and ecological safety.[4,5]

Among the analytes of interest, Ag(I) occupies a distinctive position at the confluence of environmental toxicity and economic significance.[6,7] Silver nanoparticles and ions find extensive applications in fields such as photography, electronics, and antimicrobial coatings; however, their release into aquatic ecosystems presents substantial risks. Ag(I) is acutely toxic to aquatic organisms even at minimal concentrations and can cause argyria, a permanent skin pigmentation condition, in humans following prolonged exposure.[8] Nevertheless, when considered within the framework of the circular economy, silver is identified as a critical material. The diminishing availability of natural ores calls for a fundamental shift from mere extraction to the recovery of silver from secondary sources, such as

[a]Department of Chemistry, College of Science and Arts, King Abdulaziz University, Rabigh, Saudi Arabia. E-mail: aamallehabi@kau.edu.sa
[b]Department of Chemistry, Faculty of Science and Arts, Najran University, Najran, Saudi Arabia. E-mail: azzaattia81@yahoo.com
[c]Chemistry Department, Faculty of Science, Islamic University of Madinah, Madinah, 42351, Saudi Arabia. E-mail: mssaeed@iu.edu.sa; talraddadi@iu.edu.sa; ashahat@aucegypt.edu
[d]Institut für Chemie und Biochemie, Anorganische Chemie, Freie Universität Berlin, Fabeckstraße 34-36, 14195 Berlin, Germany. E-mail: b.sarkar@fu-berlin.de
[e]Department of Chemistry, Faculty of Science, Suez University, 43533 Suez, Egypt. E-mail: reda.elshaarawy@suezuniv.edu.eg; Tel: +20 1002535379
[f]Department of Petrochemical, Egyptian Petroleum Research Institute (EPRI), Nasr City, Cairo 11727, Egypt. E-mail: mashenashen@gmail.com

leachates derived from electronic waste, urban mining. Consequently, the development of sensing materials that can selectively capture Ag(I) for subsequent recovery represents a sustainable solution of considerable value.[9,10]

Concurrently, Fe(III), while being a crucial trace element for the synthesis of hemoglobin and various metabolic functions, poses a significant environmental threat at heightened concentrations.[11] An excessive presence of ferric ions has been associated with neurodegenerative conditions, such as Parkinson's and Alzheimer's diseases, in addition to hemochromatosis.[12] In the environment, if iron is released in an uncontrolled manner, it can cause eutrophication and the Fenton reaction, which produces ROS, causing oxidative stress in aquatic organisms. Moreover, the prevalence of Fe(III) frequently complicates the detection of other trace metals, thus necessitating its selective monitoring for precise environmental assessment.[13]

Traditional spectrometric methodologies, including atomic absorption spectroscopy (AAS), inductively coupled plasma mass spectrometry (ICP-MS), and X-ray fluorescence (XRF), offer high sensitivity; however, they are constrained by notable operational limitations.[14,15] These techniques require large, complex sample preparation procedures, costly equipment, and highly trained personnel, making them unsuitable for prompt, on-site analysis in resource-limited settings. This technological gap has prompted a transformative shift towards solid-phase optical sensors, particularly spectrophotometric probes, which offer an appealing combination of cost efficiency, portability, and rapid visual detection.[16,17] Nevertheless, the commercial feasibility of such sensors is often undermined by reliance on costly synthetic supports and non-renewable precursors, underscoring the urgent need for sustainable, eco-friendly material alternatives.

In this context, nanosilica derived from agricultural biomass has emerged as a highly effective support matrix for chemical-sensing applications.[18] In contrast to commercially produced silica, which is synthesized from energy-intensive alkoxysilanes such as tetraethyl orthosilicate (TEOS), biogenic silica obtained from rice husk (RH), a widely available agricultural byproduct, provides a sustainable and cost-effective alternative.[19,20] This biogenic silica is characterized by its naturally high surface area and a silanol-rich surface that can be readily modified.[21] Solid-state sensors based on such porous supports are of paramount importance as they enable rapid, on-site real-time monitoring without the need for complex sampling or the use of hazardous organic solvents typical of solution-phase assays. Consequently, immobilizing organic chromophores, including Schiff bases, onto this porous scaffold yields a hybrid inorganic–organic sensor that combines the mechanical stability of the silica substrate with the high selectivity of the ligand.[22] Although various silica-based sensors have been documented, many are hindered by shortcomings such as slow response times, instability due to leaching, or an inability to effectively differentiate between competing ions in complex matrices, thereby limiting their practical application.[23] A closely related contribution was recently reported by Mazi *et al.*,[24] who fabricated PR@RHS by immobilizing the azo dye para red onto rice husk-derived silica for the dual detection of Hg(II) and Ag(I), achieving LODs of 13.67 ppb and 10.25 ppb, respectively. The present work is distinguished from that report on four specific grounds. First, the sensing ligand employed here the brominated bis-imine Schiff base BNP belongs to an entirely different chemical class (azomethine/imine chemistry) compared to the azo chromophore (diazene chemistry) used by Mazi *et al.*, resulting in a fundamentally different coordination chemistry and optical response mechanism. Second, the target analyte pair is distinct: BNP@RHNS is designed for the selective detection of Ag(I) and Fe(III), whereas PR@RHS targets Hg(II) and Ag(I). The recognition of Fe(III) *via* the phenolate-imine N_2O_2 chelation cavity of BNP represents a different mechanistic and selectivity challenge from Hg(II) detection *via* ON-chelation reported by Mazi *et al.* Third, the immobilization strategy differs BNP is loaded onto RHNS *via* impregnation driven by hydrogen bonding, π–π stacking, and acid–base interactions with surface silanols, whereas Mazi *et al.* employ an azo-based formation process with a possible covalent component. Fourth, the application scope differs in that the present work focuses on Ag(I) recovery from electronic waste leachates and Fe(III) monitoring in environmental water matrices, while Mazi *et al.* demonstrate Hg(II) quantification in cosmetic formulations.

Addressing these limitations, this work reports the design and fabrication of a new, robust spectrophotometric sensor, BNP@RHNS, for the dual detection of Ag^+ and Fe^{3+} ions. By valorizing rice husk waste into a high-value mesoporous support, we present a waste-to-wealth approach that aligns with the principles of green chemistry. Distinct from previous studies, this sensor integrates a bulky brominated Schiff base ligand that utilizes a specific N_2O_2 donor cavity to achieve detection limits LOD 0.185 ppm and 0.247 ppm for Ag^+ and Fe^{3+}, respectively, and exceptional selectivity against common interferents. The study provides a comprehensive molecule-to-application analysis, validates the sensing mechanism using DFT calculations, and demonstrates the sensor's practical utility in real-world environmental water samples. This dual-functional platform represents a significant advancement in the development of sustainable, rapid, and chemically stable tools for heavy-metal monitoring.

2 Material and methods

2.1 Materials and reagents

Raw rice husks were got from a local agricultural processing facility, washed thoroughly with deionized water to eliminate adhering dust and soil, and dried at 100 °C before use. For the synthesis of the ligand and nanocomposite, 2-hydroxy-1-naphthaldehyde (98%) and 4-bromo-1,2-diaminobenzene (97%) were purchased from Sigma-Aldrich. Analytical-grade solvents, including absolute ethanol, methanol, and acetone, together with sodium hydroxide (NaOH) pellets and hydrochloric acid (HCl, 37%), were obtained from Merck and used without further purification. Stock solutions (1000 ppm) of Ag(I) and Fe(III) were prepared by dissolving appropriate amounts of silver nitrate ($AgNO_3$) and ferric chloride hexahydrate ($FeCl_3 \cdot 6H_2O$) in deionized water. Solutions of potential interfering

ions, including Au^{3+}, Ca^{2+}, Cd^{2+}, Ce^{3+}, Co^{2+}, Cr^{3+}, Mg^{2+}, Hg^{2+}, Cu^{2+}, Mn^{2+}, Ni^{2+}, Pb^{2+}, Pd^{2+}, and Zn^{2+}, were prepared from their respective chloride salts. Universal buffer solutions ranging from pH 2.0 to 9.0 were prepared using mixtures of boric acid, phosphoric acid, and acetic acid, adjusted with NaOH or HCl, to evaluate the pH-dependent sensor response. Ultrapure water (18.2 MΩ cm), generated by a Milli-Q system, was used to create all aqueous solutions.

2.2 Synthesis rice husk-derived nanosilica (RHNS)

The extraction of nanosilica from rice husk was achieved *via* a modified thermochemical sol–gel route designed to maximize surface silanol density while eliminating metallic impurities, as illustrated in Scheme 1.[18,25–28] Initially, the washed rice husks were subjected to acid leaching by refluxing in 1.0 M HCl at 80 °C for 2 h. This pre-treatment step is critical for solubilizing trace metallic ions that otherwise induce crystallization and reduce the surface area of the final silica. The acid-treated husks were washed with deionized water. This continued until they were neutral. Then, they were dried and calcined. Calcination occurred in a muffle furnace at 700 °C for 6 hours. The heating rate was 5 °C per minute. The resulting white rice husk ash (RHA) was collected. It was composed mainly of amorphous silica. It was collected for extraction. To isolate the nanosilica, the RHA was dispersed in 2.5 M NaOH and stirred vigorously at 90 °C for 3 h to form water-soluble sodium silicate (Na_2SiO_3). The solution was filtered to remove undissolved carbon residue. Nanosilica was precipitated by drop-wise addition of 1.0 M HCl to the filtrate under constant stirring until the pH reached 7.0, yielding a pristine white aqua gel. The gel was aged for 18 h to strengthen the silica network, then centrifuged and repeatedly washed with warm deionized water to remove NaCl by-products. Finally, the product was dried at 80 °C for 24 h and pulverised to get a fine, white powder of RHNS.

2.3 Synthesis of Br-naphthophen (BNP) ligand

The new Schiff base ligand, Br-naphthophen ligand, was synthesized *via* a standard Schiff base condensation reaction as shown in Scheme 2.[29,30] In a typical procedure, 10 mmol of 4-bromobenzene-1,2-diamine was mixed with 20 mmol of 2-hydroxy-1-naphthaldehyde in 30 mL of ethanol. A light orange precipitate formed immediately after mixing, and the contents were refluxed for 3 h. The solid product was subsequently isolated by filtration, washed twice with cold ethanol (2 × 5 mL) to remove impurities, and dried, yielding the pure ligand. Yield: 3.6 g, 73.7%. M.p. 255–257 °C. ^{1}H-NMR (DMSO-D_6): 6.7–7.9 (m, aromatic protons, 15H), 8.27 (s, HC=N, 2H), 9.86 (bs, OH, 2H). ^{13}C-NMR (DMSO-D_6): 119.6–165.8. MS (EI): *m*/*z* 494.09. Anal. calcd. for $C_{28}H_{19Br}N_2O_2$: C 67.89; H 4.87; N 5.66. Found: C 67.65; H 4.56; N 5.81.

2.4 Fabrication of the BNP@RHNS sensor

BNP was immobilized onto the RHNS matrix *via in situ* impregnation by taking advantage of the extensive surface activity of the silanol groups on silica. After that, the RHNS was pre-activated at 120 °C for 2 h to remove physisorbed water, which guarantees maximal accessibility of the pore channels before synthesis. For the general synthesis procedure, 1.0 g RHNS was dispersed into 100 mL of anhydrous ethanol under ultra-sonication for 30 min to achieve homogeneous particle distribution. A homogeneous solution was prepared by dissolving 0.5 g of the synthesized Br-naphthophen ligand in 50 mL of absolute ethanol, and this solution was then slowly introduced into the silica suspension while it was continuously stirred. Mechanical stirring at 300 rpm was used throughout the 8 hour immobilization process, carried out at 60 °C under reflux. To enhance ligand loading, parameters like ligand concentration ratio, reaction duration, and temperature were thoroughly reviewed. This process ensured maximum surface coverage was achieved while maintaining the integrity of the sensing function. This in turn allowed for both ideal ligand-to-

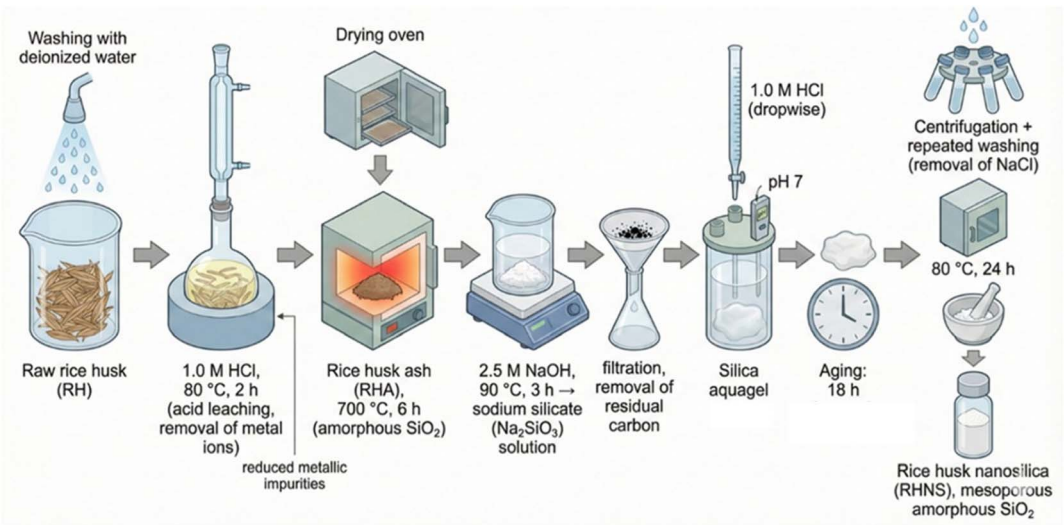

Scheme 1 Synthesis of RHNS *via* the thermochemical sol–gel route.

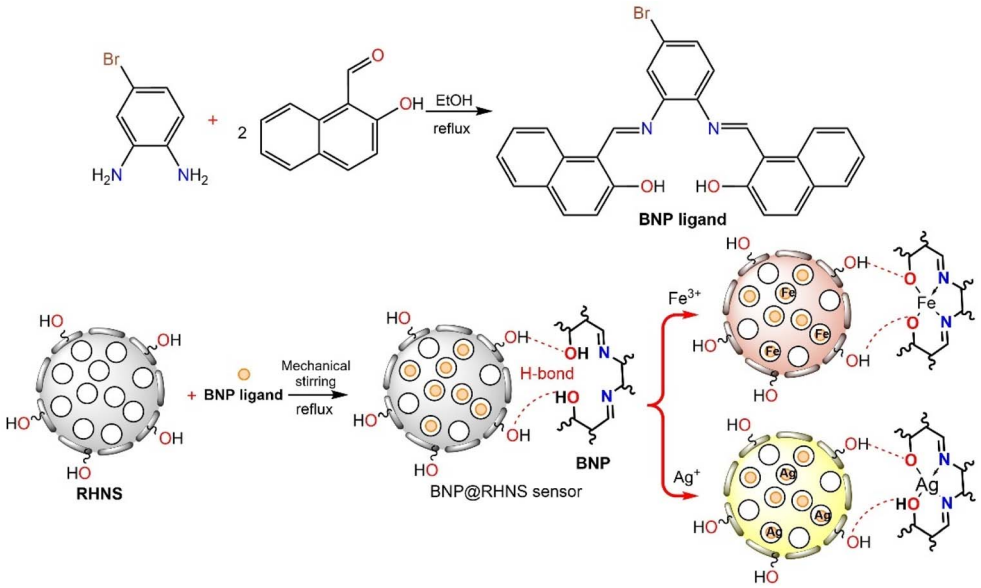

Scheme 2 Synthesis of the BNP ligand and BNP@RHNS sensor as well as optical sensing of Ag^+ and Fe^{3+} ions.

silica binding efficiency and structural integrity. After the immobilization process was completed, the BNP@RHNS Sensor was separated by centrifugation at a speed of 8000 rpm for 15 min. The material was washed with ethanol and deionized water to remove additional unbound ligand. Complete removal and stabilization of structure was achieved by vacuum drying at 50 °C for 24 h in the final purification step.

2.5 Spectrophotometric sensing studies

To evaluate the sensing ability of this sensor, spectrophotometric monitoring was utilized in a batch system, and to ensure full experimental reproducibility, the BNP@RHNS sensor was stored as a dry solid powder following the final vacuum drying purification stage. The material was maintained in a glass desiccator at a regulated room temperature of 25 °C, with the relative humidity (RH) kept below 10% using anhydrous silica gel to prevent atmospheric moisture-induced hydrolysis of the sensitive azomethine linkages. To mitigate the risk of photodegradation of the naphthalene-based Schiff base, the desiccator was placed in a dark environment protected from direct ambient light, and storage was conducted at ambient pressure rather than under vacuum to accurately simulate realistic laboratory shelf-life conditions. The sensor was divided into 20 mL of a universal buffer and sonicated for 2 min to generate a uniform suspension for an ordinary assay. Then appropriate aliquots of the metal ion stock solutions (Ag^+ or Fe^{3+}) were added to reach the final concentrations desired. To promote mass transfer, the reaction mixture was vortexed for 40 s and allowed to equilibrate at room temperature. Absorbance measurements were performed in the spectral range of 200–600 nm with a reagent blank serving as the reference. In the case of Ag^+ and Fe^{3+}, quantitative determination was carried out at their respective λ_{max} (250 nm for Ag^+; 270 nm for Fe^{3+}). To investigate the selectivity, excesses of alternative interfering ions were added into the sensing system under the same conditions.

2.6 Analytical studies

2.6.1 Determination of Ag^+ and Fe^{3+} ions in real water samples. The performance of BNP@RHNS sensor for environmental monitoring Ag^+ and Fe^{3+} ions, was checked on tap water by spectrophotometric method. Each sample was filtered through a 0.45 μm cellulose acetate membrane to remove suspended solids, and the pH of each sample was then adjusted using dilute buffer solutions prior to analysis. Because environmental samples are likely to exhibit matrix interferences, the Standard Addition Method was utilized. For this purpose, known concentrations of Ag^+ and Fe^{3+} were spiked into the pretreated water samples, from which recovery rates were determined based on the obtained calibration curves. The performance of the proposed sensor was verified by statistically comparing its readings with those obtained by ICP-OES, which was used as the reference method. Precision and accuracy were assessed through relative standard deviation (RSD) and percentage recovery, calculated from three replicate measurements ($n = 3$).

2.6.2 Estimation of Ag^+ in E-waste. The experimental preconditions involved a specific amount of coarse waste printed circuit boards (WPCBs) retrieved from various discarded computer equipment. WPCBs in powder were leached for 8 h using a solution of 2.0 M H_2SO_4 and 0.2 M H_2O_2 at 90 °C. Next, the mixture was filtered, and the remainder was oxidized with 50% HNO_3 at 70 °C for 5 h to solubilize a broad spectrum of ions. The pH of the filtrate was adjusted to 2.0 with 2 M NaOH and filtered again to separate Al^{3+} and Sn^{4+} ions from your filtrate. The mixture was then subjected to HCl/HNO_3 treatment (3 : 1) at 70 °C for about 3 hours, resulting in the Ag^+-rich

solution. Then, the pH was increased using 2 M NaOH for their detection.

3 Result and discussion

3.1 Insight into the synthesis process

RHNS was synthesized using a thermochemical sol–gel method involving the combination of acid leaching, calcination, and controlled precipitation to yield amorphous silica with high surface areas and silanol-rich properties (*cf.* Scheme 1). Acid washing of RH removes metal impurities, calcination transitions the organic matrix into silica rich ash and NaOH extraction with HCl induced gelation and aging promotes Si–OH formation and growth of a Si–O–Si network all while retaining a nanostructured templating framework amenable to ligand anchoring.

The Br-naphthoPhen (BNP) ligand is formed *via* a classical Schiff base condensation between 4-bromobenzene-1,2-diamine and 2-hydroxy-1-naphthaldehyde (*cf.* Scheme 2), yielding a conjugated bis-imine with phenolic O and imine N donors, validated by its diagnostic imine NMR signals, molecular-ion peak, and elemental analysis, designed to facilitate chelation based optical sensing of Ag(I) and Fe(III).

Eventually, BNP@RHNS is prepared by the impregnation of thermally activated RHNS in an ethanolic solution containing BNP, whereupon the ligand adsorbs within the mesoporous networks by hydrogen bonding, π–π and acid–base interactions with surface silanols. Long-careful stirring/reflux under solvent conditions then comprehensive washing and mild vacuum drying result in a highly homogeneous, low leaching layer of BNP on RHNS that retains porosity, forming a stable, water-dispersible spectrophotometric probe.

3.2 Structural and morphological characterization

3.2.1 Morphological analysis. FE-SEM and TEM characterized the topography of the surface and internal nanostructure. FE-SEM micrographs of pristine RHNS reveal agglomerates with irregular shapes and rough surfaces (Fig. 1A), reflective of rapid nucleation of silica during sol–gel precipitation and a wealth of surface-active sites for functionalization. The connectivity of the support, as evidenced by the morphological structure, was intact post immobilization of the Br-naphthophen ligand. As shown in Fig. 1B, the SEM images of BNP@RHNS exhibited a similar particulate shape to that observed for the host matrix, but with a more compacted and smoother surface texture. This alteration is attributed to the creation of a thin layer of organic Schiff base ligand on both the exterior surface and the pore openings.

To gain deeper insight into the internal pore architecture, TEM analysis was conducted. The TEM image of pristine RHNS clearly illustrates a disordered mesoporous network, typical of amorphous silica derived from agricultural waste (Fig. 1C). The particles appear relatively transparent to the electron beam, confirming their porous nature. In contrast, the TEM micrograph of the BNP@RHNS sensor Fig. 1D, reveals regions of darker contrast and increased density throughout the silica matrix. This variation in electron density provides direct visual evidence that the heavy organic ligand molecules have successfully diffused into and occupied the mesoporous channels, rather than merely coating the external surface.

3.2.2 BET surface area analysis. The effect of ligand immobilization on the textural parameters of the nanosilica support was quantified by N_2 adsorption–desorption measurements at 77 K. The adsorption isotherms for both the pristine RHNS and the BNP@RHNS sensor are presented in Fig. 2A. Pristine RHNS exhibits a Type IV according to IUPAC classification, possessing a H3 hysteresis loop in the relative pressures P/P_0. This profile represents a typical mesoporous morphology with cylindrical pore channels, which is common for silica-based materials synthesized through the sol–gel route. Functionalization of the copolymer with Br-naphthophen ligand resulted in an isotherm that was similar to that of host, confirming that the pore architecture remained intact. However, a distinct decrease in the volume of adsorbed nitrogen was observed across the entire pressure range. In summary, the Brunauer–Emmett–Teller (BET) specific surface area (S_{BET}) decreased significantly from 383.71 $m^2\ g^{-1}$ to 287.80 $m^2\ g^{-1}$. Concurrently, the total pore volume decreased from 1.057 $cm^3\ g^{-1}$ to 0.972 $cm^3\ g^{-1}$. This attenuation in textural properties is not attributable to the collapse of the silica skeleton but rather provides quantitative evidence for the 'pore-filling' mechanism.

3.2.3 Phase purity and crystallinity. The crystallographic structure and phase purity of the fabricated RHNS and BNP@RHNS sensor were explored through an X-ray diffraction (XRD) experiment, with patterns shown in Fig. 2B. The diffractogram of pristine RHNS exhibits a broad, diffuse halo centered at $2\theta = 23°$, a well-known signature of amorphous silica (SiO_2), which indicates the presence of a disordered structure with short-range order but no long-range order. The lack of well-defined sharp diffraction peaks expresses that thermal calcination at 700 °C removed organic lignocellulosic components and then caused no phase transition to crystalline polymorphs cristobalite or tridymite, which occurred at higher temperatures (>800 °C). The XRD pattern of Br-naphthophen ligand immobilized on silica retained the characteristic hump typical of amorphous silica host, indicating that the modification process did not disrupt the silicate framework. In the XRD pattern of the nanocomposite, we don't see distinctive sharp diffraction peaks corresponding to the pure crystalline Br-naphthophen ligand, which implies that the organic molecules are in molecular dispersion in the mesoporous channels or exist in an amorphous state due to pore confinement. This phase non-crystallization is a benefit for sensing applications by allowing sites in a positional monolayer-wise rather than aggregates of ligands in the bulk.

3.2.4 ^{1}H NMR spectroscopy. The BNP ^{1}H NMR spectrum (Fig. 3A) is entirely consistent with the proposed family of symmetric bis-Schiff base structures based on 4-bromobenzene-1,2-diamine and 2-hydroxy-1-naphthaldehyde. The signals at δ 9.86 (2H) and 8.54 (2H), which appears as a pair of singles, were assigned to the strongly hydrogen-bonded phenolic OH and imine (HC═N) protons, confirming successful condensation of the aldehyde and diamine, leading to two azomethine

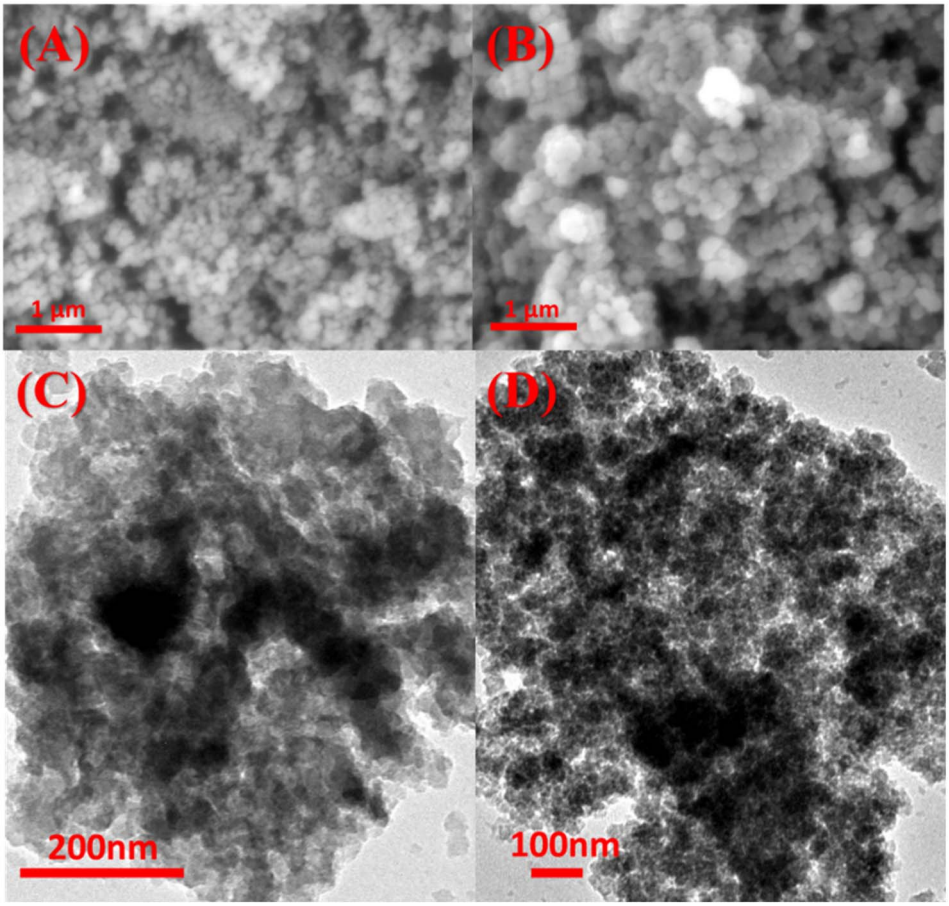

Fig. 1 (A) FE-SEM image of pristine RHNS; (B) FE-SEM image of the BNP@RHNS sensor; (C) TEM micrograph of pristine RHNS; and (D) TEM micrograph of the sensor.

centres characteristic for Schiff bases based on naphthalene. Aromatic region (δ 6.99–7.72) exhibits a series of well-resolved doublets, doublet-of-doublets and triplet integrating to the expected 15 protons with coupling constants ($J \approx 2$–9 Hz) consistent with *ortho*- and *meta*-substituted benzene and naphthalene rings, underlying conjugated π-extended architecture necessary for efficient metal-ions recognition. A clean baseline, with no residual aldehydic or amino resonances, corroborates the high purity and complete imine formation consistent with literature findings related to N_2O_2-donor naphthyl Schiff bases employed as chromogenic/fluorogenic chemosensors.

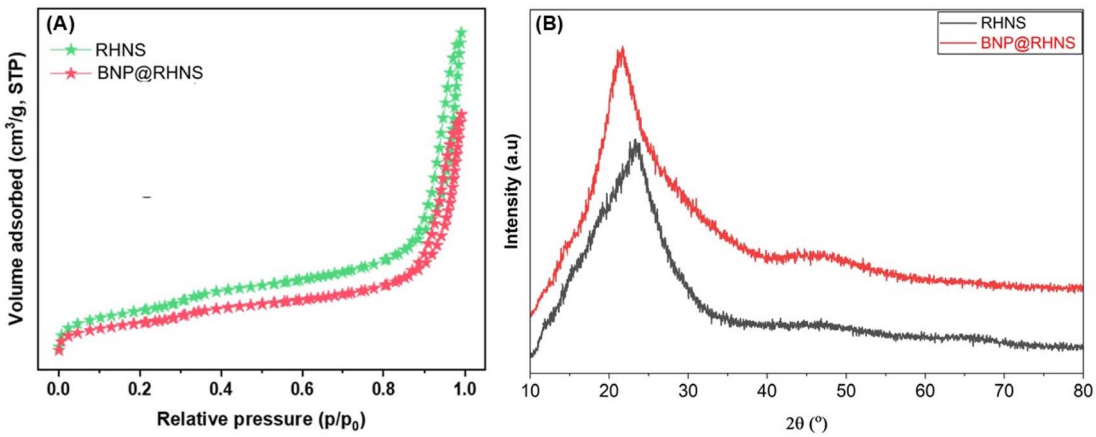

Fig. 2 (A) N_2 adsorption–desorption isotherm analysis, and (B) XRD analysis pattern of the RHNS and BNP@RHNS sensor.

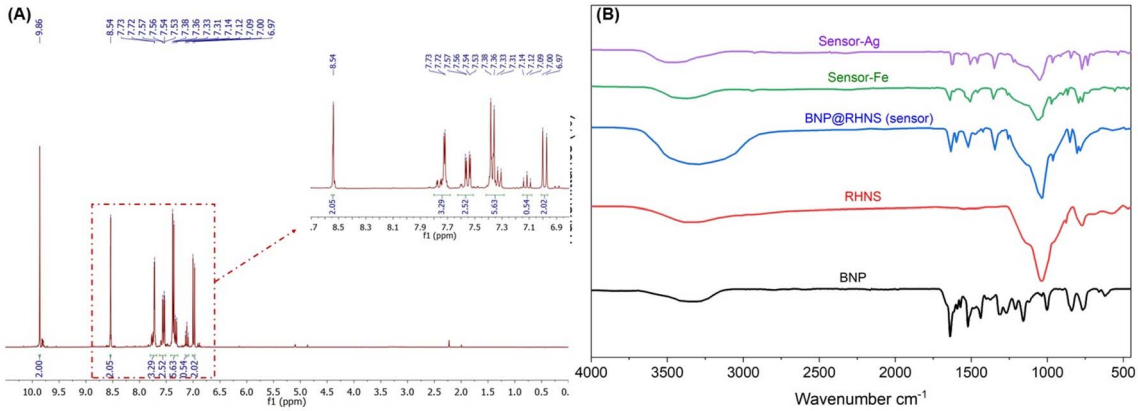

Fig. 3 (A) ^{1}H NMR spectrum of BNP ligand. (B) FTIR spectra of RHNS and the BNP@RHNS sensor.

3.2.5 FTIR spectroscopy. Fourier transform infrared (FTIR) spectroscopy was utilized to monitor the stepwise fabrication of the sensor and to elucidate the coordination mechanism with the target analytes. The comparative spectra of the pristine BNP ligand, RHNS, the BNP@RHNS sensor, and the metal-loaded composites are presented in Fig. 3B. The spectrum of the pure RHNS displays the characteristic vibrational signature of the inorganic silica support. The main, wide band at 1080 cm^{-1} is attributed to the asymmetric stretching of the siloxane (Si–O–Si) structure. The symmetric stretching of Si–O bonds is indicated by additional bands at 800 cm^{-1}, while the bending modes are shown at 460 cm^{-1}. Surface silanol groups and physisorbed water molecules exhibit O–H stretching vibrations, resulting in a broad absorption band from 3200 to 3550 cm^{-1}. Upon immobilization of the ligand, new organic signatures appear superimposed on the silica background. A distinct peak emerges at 1653 cm^{-1}, corresponding to the azomethine (–C=N–) stretching vibration, which confirms the successful entrapment of the Schiff base ligand. Weak bands in the region of 1450–1600 cm^{-1} are attributed to the aromatic C=C skeletal vibrations of the naphthalene and benzene rings. The retention of the silica framework peaks confirms that the immobilization process did not degrade the support structure. Significant spectral shifts are observed in the metal-loaded sensors, providing direct evidence of chelation. For the Ag^{+} loaded sensor, the characteristic azomethine (–C=N–) band exhibits a redshift from 1653 cm^{-1} to 1635 cm^{-1}, accompanied by a decrease in peak intensity. This shift indicates the donation of the lone pair of electrons from the imine nitrogen to the empty orbitals of the Ag^{+} ion. For the Fe^{3+} loaded sensor, a similar shift is observed for the –C=N– band to 1635 cm^{-1}. Furthermore, subtle changes in the phenolic C–O stretching region (1250–1280 cm^{-1}) suggest the participation of the naphthalene hydroxyl groups in the coordination sphere. These spectral variations confirm that the adsorption mechanism is not merely physical entrapment but involves chemical coordination, with the N_2–O_2 donor cavity of the Br-naphthophen ligand acting as a chelating site for the metal ions.

3.3 Optimization of sensing conditions

3.3.1 Effect of solution pH on sensor response. The pH of the aqueous medium is a paramount parameter governing the chelation efficiency, as it simultaneously influences the protonation state of the ligand's donor sites (–N and –OH) and the chemical speciation of the metal.[31] To establish the thermodynamic optimum for sensing, the spectrophotometric response of the BNP@RHNS sensor toward Ag^{+} and Fe^{3+} was systematically evaluated over the pH range 2.0–9.0 using universal buffer solutions. The results, illustrated in Fig. 4A, reveal distinct pH-dependent sensing profiles for the two analytes. For Ag^{+}, the optimum sensing response was achieved at a slightly higher pH value of 6.2. At lower pH the high concentration of hydronium ions (H_3O^{+}) competes aggressively with the borderline soft acid Ag^{+} for the nitrogen donor sites, inhibiting the formation of the Ag–N bond. At higher pH (pH > 8.0), the signal intensity declined due to the formation of silver oxide precipitates (Ag_2O) or soluble hydroxy-complexes ($Ag(OH)_2^{-}$), which do not interact effectively with the immobilized ligand. For Fe^{3+}, the sensor exhibited a sharp maximum absorbance at pH 3.6. In the acidic region (pH < 3.0): the sensing response was significantly diminished. This is attributed to the competitive protonation of the imine nitrogen (–C=NH^{+}) and the phenolic oxygen, which creates an electrostatic repulsion barrier effectively blocking the coordination of the positively charged Fe^{3+} ions. In the near-neutral/alkaline region (pH > 5.0): a precipitous drop in signal was observed. This behaviour is consistent with the hydrolysis of ferric ions to form insoluble hydroxide species, $Fe(OH)^{2+}$ and $Fe(OH)_3$. The formation of these hydroxylated species reduces the concentration of free Fe^{3+} available for complexation with the Br-naphthophen ligand. Consequently, based on these distinct maxima, pH 6.2 and pH 3.6 were selected as the standardized conditions for Ag^{+} and Fe^{3+}, respectively, for all subsequent selectivity and sensitivity assays.

3.3.2 Effect of sensor dosage. Fig. 4B shows the effect of the sensor loading (5–40 mg) on absorbance intensity towards selecting a cost and time-effective nanocomposite dosage for quantitative assay under controlled analyte concentration and

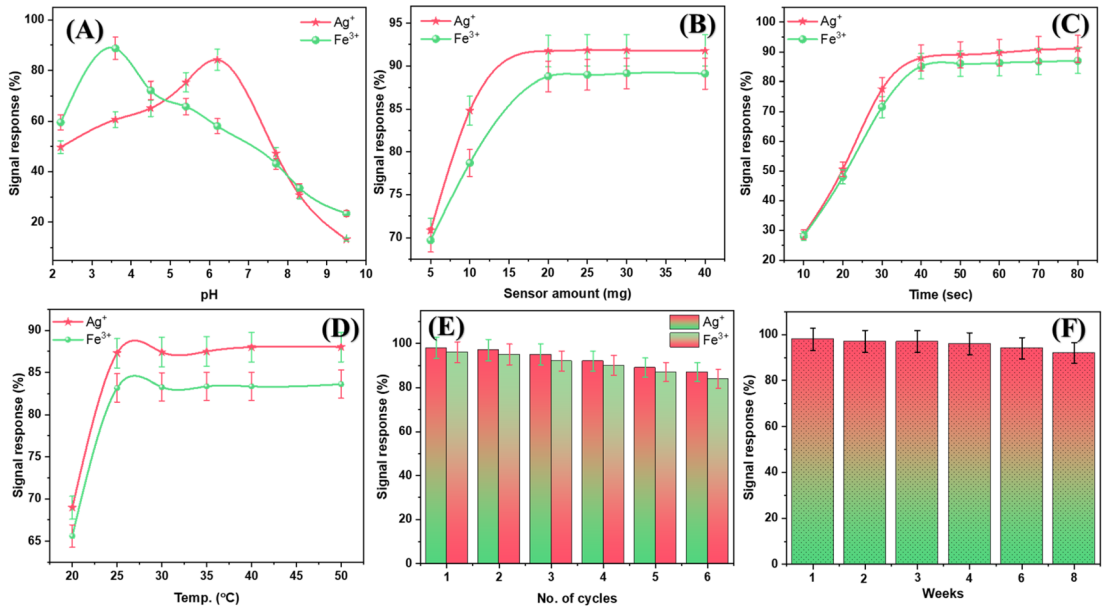

Fig. 4 Analytical parameters assessment for the recognition of Ag^+ and Fe^{3+} ions with the BNP@RHNS sensor, in terms of signal response (%) as a function of pH solution (A), BNP@RHNS sensor amount (B), reaction time (C) reaction temperature (D), reusability (E) and stability studies (F).

pH. For Ag^+ detection, the analytical signal sharply increased at 20 mg as a direct consequence of the increasing number of surface-accessible N_2O_2 binding sites, which facilitates metal ion uptake and complexation. For Fe^{3+}, a similar trend was observed with a maximum absorbed plateau at 20 mg. However, beyond these optimum mass values, further addition of the sensor did not yield a significant increase in absorbance; in fact, a slight baseline instability was noted at higher loadings. This saturation plateau indicates that the metal ion concentration becomes the limiting factor rather than the availability of adsorption sites. Furthermore, excessive solid content typically induces particle agglomeration and increases the turbidity of the suspension, leading to light scattering that interferes with accurate spectrophotometric measurements.

3.3.3 Effect of contact time. For any practical on-site analytical device, a rapid and stable response is a prerequisite. The temporal evolution of the spectrophotometric signal was monitored to determine the response time, defined as the time required for the sensor to reach a stable absorbance plateau. Dynamic response profiles for Ag^+ and Fe^{3+} sensing were recorded by measuring absorbance at intervals from 0 to 80 s, as shown in Fig. 4C. The findings indicate that the spectrophotometric signal increased rapidly within a 40 s interval. Following this initial period, the signal reached a plateau after roughly 40 s, at which point no notable further enhancement in the spectrophotometric signal was detected.

3.3.4 Temperature-dependence study. To better understand the energetic characteristics of the binding interactions and evaluate its stability under different thermal conditions, the absorbance response for Ag^+ and Fe^{3+} was measured in the temperature range from 20 to 50 °C. As depicted in Fig. 4D, at higher temperatures, an increase in analytical signal intensity occurred as temperature increased. The trend reveals a positive correlation between temperature and Q which consequently states that the metal ion complexation onto the BNP@RHNS surface is an endotherm process.

3.3.5 BNP@RHNS sensor reusability and regeneration studies. To evaluate the economic feasibility and sustainability of the proposed sensor, the regeneration capability of the BNP@RHNS sensor was assessed over multiple adsorption–desorption cycles. The reversibility of the complexation process relies on a pH-dependent binding mechanism; because metal–ligand coordination is inhibited in highly acidic media, acid washing was used to strip the bound metal ions. In a typical regeneration protocol, the metal-loaded sensor was collected after the detection phase, washed with deionized water, and treated with 0.1 M HCl for 15 min under mild agitation. The regenerated sensor was then neutralized with a dilute buffer, washed, and reused for the subsequent spectrophotometric determination of Ag^+ and Fe^{3+}. As shown in Fig. 4E, the sensor retained its high sensing performance for up to 6 consecutive cycles. The response began to decline gradually after the third cycle. This could be due to the partial leaching of the physisorbed ligand or slight mechanical wear of the silica support from repeated centrifugation. The quantitative data for six consecutive adsorption–desorption cycles are summarized in Table S3. These results demonstrate that while a gradual decline in performance is observed after the third cycle, likely due to minor ligand leaching or mechanical wear, the BNP@RHNS sensor remains well within our defined acceptance threshold through the sixth cycle. Nevertheless, the recovery of >80% of the initial capacity after multiple runs confirms the robust anchoring of the Br-naphthophen ligand and highlights the potential of this sensor for cost-effective, long-term environmental monitoring applications.

3.3.6 Long-term storage stability. The shelf-life of the sensor was assessed by storing a batch of the synthesized sensor in a desiccator at room temperature (25 °C) for 8 weeks. To ensure experimental consistency, the desiccator was equipped with an active desiccant to maintain low relative humidity and kept in a dark cabinet to prevent direct light exposure. The sensing performance was periodically evaluated by measuring the absorbance response toward standard concentrations of Ag^{+} and Fe^{3+}. As illustrated in Fig. 4F, the sensor exhibited remarkable stability, retaining over 90% of its initial sensing capacity after 8 weeks of storage. No significant drift in the baseline signal or alteration in the colorimetric response was observed. This extended shelf-life is attributed to the encapsulation of the organic ligand within the nanosilica channels, which shields the azomethine (–C═N–) linkages from hydrolytic degradation and oxidative attack by atmospheric moisture.

3.4 Spectrophotometric detection and analytical performance

3.4.1 Spectral features and sensing mechanism. The qualitative recognition capability of the BNP@RHNS sensor was initially investigated by monitoring changes in the UV-Vis absorption spectrum upon addition of various metal ions.[32] The blank sensor suspension exhibited negligible background absorbance in the visible region, as shown in Fig. 5A and D. However, the addition of Ag^{+} and Fe^{3+} ions induced distinct spectral changes. For Ag^{+}, a new absorption band appeared at $\lambda_{max} = 250$ nm.[33] This bathochromic shift is ascribed to the ligand-to-metal charge transfer (LMCT) transition, specifically involving the excitation of electrons from the filled π-orbitals of the imine nitrogen to the empty 5s orbitals of the silver ion. For Fe^{3+}, a broad, intense absorption peak emerged at $\lambda_{max} = 270$ nm. This feature is characteristic of the d–d transition of the iron center, enhanced by the strong chelation with the azomethine nitrogen and phenolic oxygen donors of the ligand. Since the optimal pH values for Ag^{+} (pH 6.2) and Fe^{3+} (pH 3.6) detection differ, quantitative analysis of both ions in a single sample is performed sequentially on two pH-adjusted aliquots of the same sample. This two-step protocol adds minimal sample preparation time and is fully compatible with standard environmental monitoring workflows.

3.4.2 Calibration curve and linearity. Calibration curves were used to assess the sensor's quantitative performance under the best experimental conditions. The absorbance intensity at the respective λ_{max} was plotted as a function of analyte concentration. The sensor exhibited a wide linear dynamic range, obeying the Beer–Lambert Law, with Ag^{+} linearity observed in the concentration range 0.18–0.80 ppm, yielding a high correlation coefficient $R^2 = 0.998$. The linear response range of Fe^{3+} was established between 0.25–0.85 ppm and $R^2 = 0.996$.

Using the standard IUPAC definitions, the LOD and LOQ were calculated to quantify the method's sensitivity.

$$\mathrm{LOD} = \frac{3\sigma}{S} \quad (1)$$

$$\mathrm{LOQ} = \frac{10\sigma}{S} \quad (2)$$

S represents the calibration curve's slope, and σ stands for the standard deviation. The calculated LOD values were 0.185 ppm

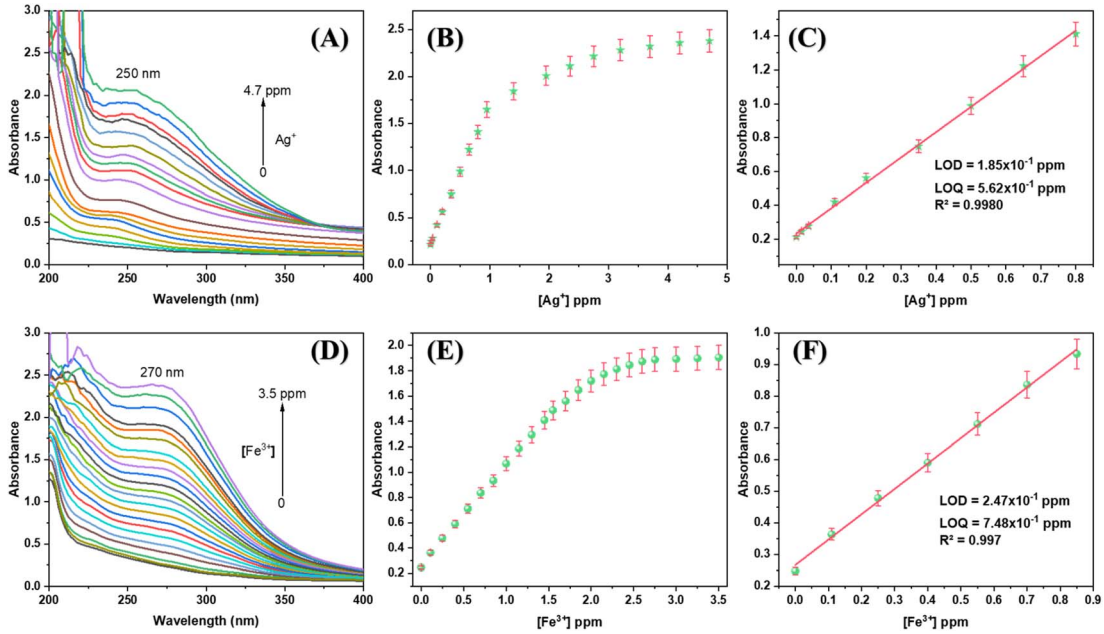

Fig. 5 Spectrophotometric sensing performance and linear calibration profiles of the BNP@RHNS sensor toward target metal ions: (A) UV-Vis absorption spectra of the sensor toward Ag^{+} ions ; (B) non-linear concentration-dependent absorbance curve for Ag^{+}; (C) linear regression calibration plot for Ag^{+}; (D) UV-Vis absorption spectra of the sensor platform with Fe^{3+} ions; (E) non-linear concentration-dependent absorbance curve for Fe^{3+}; and (F) linear calibration curve for Fe^{3+}.

for Ag^+ and 0.247 ppm for Fe^{3+}. The calculated LOD for Ag^+ (0.185 ppm) falls in the vicinity of the WHO guideline value for silver in drinking water (0.1 mg L^{-1}), and the Fe^{3+} LOD (0.247 ppm) is consistent with practically relevant environmental concentration ranges. While this value demonstrates the potential of the BNP@RHNS sensor for preliminary regulatory screening, it highlights the proximity to the recommended threshold for drinking water safety. Further sensitivity enhancement, perhaps through covalent grafting or signal amplification strategies, could be explored in future iterations to consistently operate below the WHO threshold.

3.5 Sensing mechanism

To provide a comprehensive understanding of the specific recognition behavior of the BNP@RHNS sensor towards Ag^+ and Fe^{3+}, a plausible mechanism was deduced by correlating spectrophotometric observations with FTIR spectral shifts and theoretical HSAB principles. The sensing of Ag^+ ions is primarily driven by a coordination-induced ligand-to-metal charge transfer (LMCT). The Br-naphthophen ligand possesses an electron-rich azomethine –C═N– center. According to Pearson's HSAB theory, the Ag^+ ion is a soft acid, while the imine nitrogen acts as a borderline soft base. Upon exposure to Ag^+, the lone pair of electrons on the nitrogen atom is donated to the empty 5s orbital of the silver ion. This coordination stabilizes the excited state of the ligand, causing a bathochromic shift in the absorption spectrum. This mechanism is strongly supported by the FTIR data, where the C═N stretching vibration shifted from 1653 cm^{-1} to 1635 cm^{-1}, indicating a weakening of the azomethine bond upon electron donation to Ag^+.

Recognition of Fe^{3+} proceeds *via* a chelation-enhanced d–d transition mechanism. Fe^{3+} is a hard acid with high charge density, exhibiting a strong affinity for hard oxygen donors. In the Br-naphthophen structure, the phenolic hydroxyl groups (–OH) are optimally positioned relative to the imine nitrogen to form a stable N_2O_2 coordination cavity. Upon binding, the phenolic protons are likely deprotonated, allowing the oxygen atoms to form covalent bonds with the Fe^{3+} center, while the nitrogen atoms form coordinate bonds. This creates a rigid 5- or 6-membered chelate ring, thermodynamically highly stable. The intense absorption band at ~500–600 nm corresponds to a specific charge transfer from the phenolate oxygen to the Fe^{3+} d-orbitals. Additionally, the diminished intensity of the –OH stretching band in the FTIR spectrum confirms the participation of the hydroxyl group in binding.

Overall, the RHNS matrix plays a dual role. Firstly, it spatially isolates the ligand molecules, preventing intermolecular aggregation (self-quenching) and keeping the binding sites accessible. Secondly, the high surface area of the silica enables rapid accumulation of metal ions from the bulk solution onto the sensor surface, thereby enhancing the local concentration around the ligand and lowering the detection limit.

3.6 Selectivity and interference performance

Selectivity is a critical performance parameter in the rigorous assessment of real-world chemosensors. To validate the specific recognition capability of the BNP@RHNS sensor, we investigated its spectrophotometric response to a diverse array of common coexisting metal-ion contaminants. Au^{3+}, Ca^{2+}, Cd^{2+}, Ce^{3+}, Co^{2+}, Cr^{3+}, Mg^{2+}, Hg^{2+}, Cu^{2+}, Mn^{2+}, Ni^{2+}, Pb^{2+}, Pd^{2+}, and Zn^{2+} were among the potential interfering substances examined. As illustrated in Fig. 6A and B, a distinct and robust change in absorbance intensity was observed only after the addition of the target Ag^+ and Fe^{3+} ions (0.5 ppm). In stark contrast, the spectral profile remained virtually unchanged in the presence of the BNP@RHNS sensor in contact with the interfering ions, confirming the high specificity of the ligand's N_2O_2 cavity. To quantitatively define the sensor's robustness, the tolerance limit was set to the maximum concentration of foreign ions that caused a relative deviation of less than ±5% in the absorbance measurement. As summarized in Tables S1 and S2, the BNP@RHNS sensor displayed high specificity even in the presence of substantial excesses of competing ions. Specifically, at the optimized pH values (6.2 for Ag^+ and 3.6 for Fe^{3+}), the system tolerated concentrations up to 100 ppm for the majority of tested ions, including Au^{3+}, Ca^{2+}, Cd^{2+}, Ce^{3+}, Co^{2+},

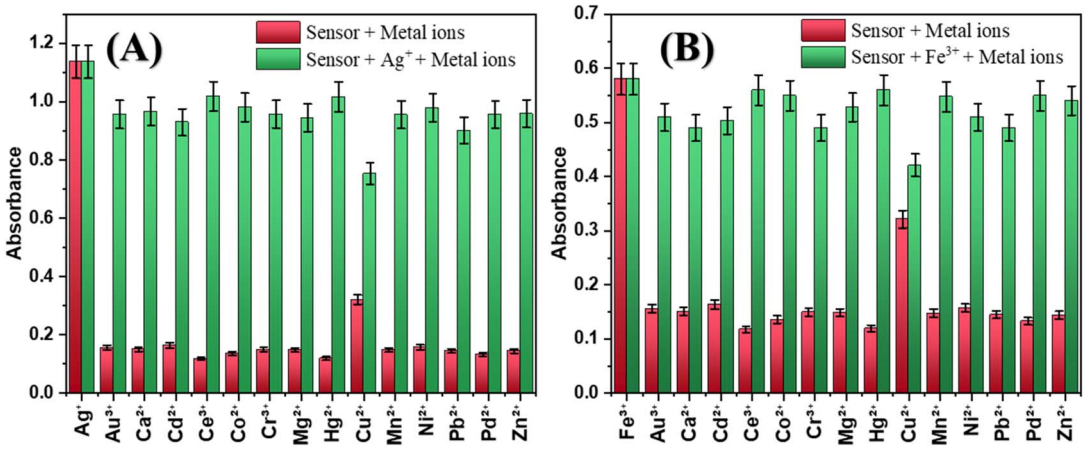

Fig. 6 Competitive selectivity and cross-interference profiles of the BNP@RHNS sensor toward target analytes in the presence of various coexisting metal ions: (A) spectrophotometric absorbance response for Ag^+; and (B) spectrophotometric absorbance response at for Fe^{3+}.

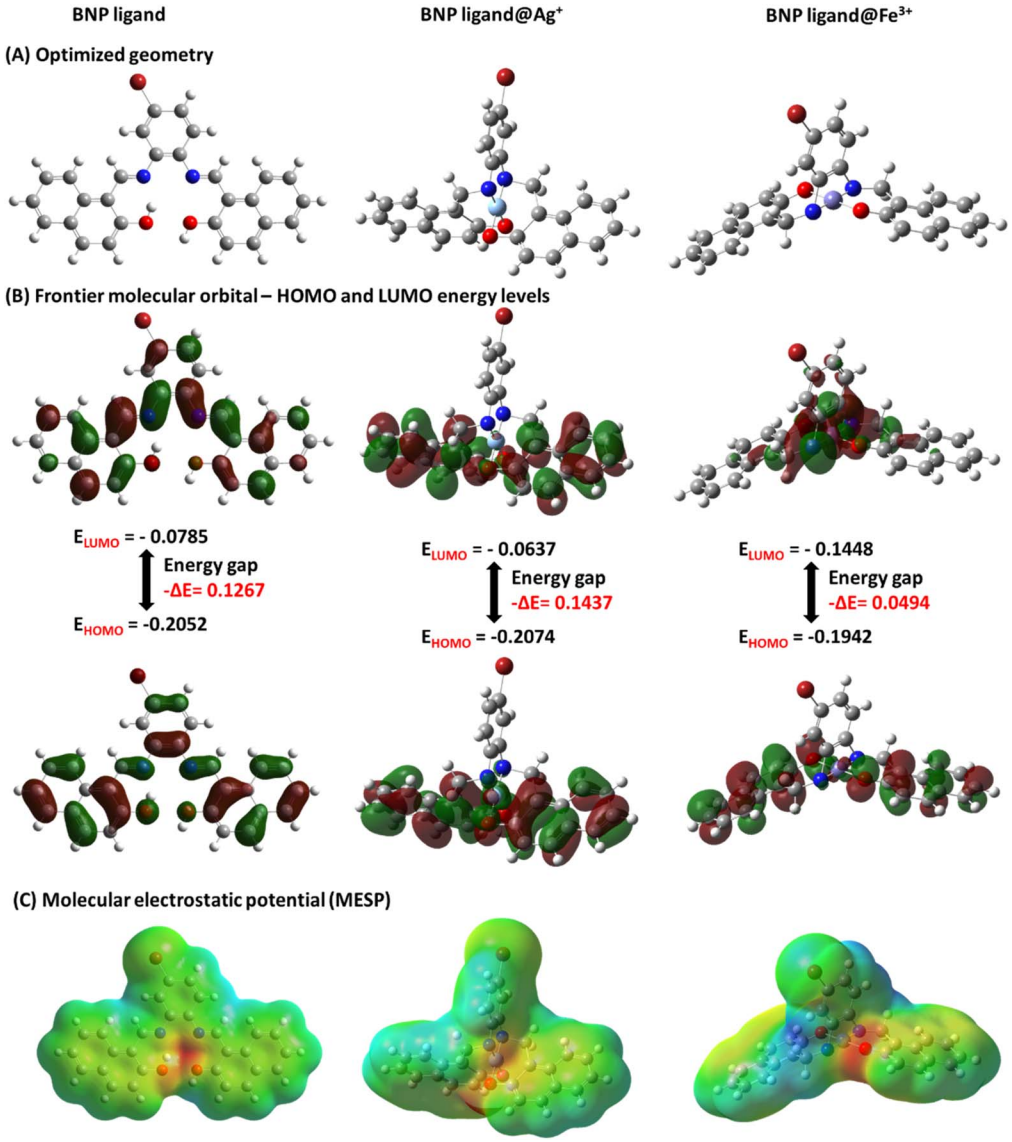

Fig. 7 (A) The optimized molecular geometries, (B) the frontier molecular orbital (FMO) analysis, and (C) the molecular electrostatic potential (MESP) maps for the BNP ligand, BNP ligand@Ag^{+}, and BNP ligand@Fe^{3+} complexes.

Cr^{3+}, Mg^{2+}, Hg^{2+}, Cu^{2+}, Mn^{2+}, Ni^{2+}, Pb^{2+}, Pd^{2+}, and Zn^{2+}. Higher tolerance limits of 125 ppm were observed for Ce^{3+} and Hg^{2+}, while Cu^{2+} exhibited a lower but still analytically significant tolerance limit of 50 ppm. These results conclusively demonstrate the sensor's capability to function as a reliable tool for dual-ion detection in complex aqueous matrices without significant cross-sensitivity.

3.7 Computational studies and theoretical validation

To provide a quantum chemical perspective on the sensing mechanism and to validate the experimental binding modes, DFT calculations were performed using the Gaussian 09 software suite. The geometries of the free Br-naphthophen ligand and its Ag^{+} and Fe^{3+} complexes were fully optimized in the gas phase using the B3LYP hybrid functional. The 6-31+G(d,p) basis set was employed for light atoms (C, H, N, O, Br), while the effective core potential (ECP) LanL2DZ basis set was utilized for the metal centers (Ag^{+} and Fe^{3+}) to account for relativistic effects. The present DFT calculations were conducted in the gas phase and therefore do not explicitly account for solvation effects operative in the aqueous buffered sensing environment, including competitive water coordination and electrostatic screening. As a consequence, the computed ΔE (HOMO–LUMO gap) values and binding energies should be interpreted as comparative trends rather than absolute thermodynamic quantities. Incorporation of the PCM implicit solvent model for single-point energy corrections or full geometry re-optimization represents a valuable future extension of this theoretical work that would provide a more quantitatively rigorous description of the metal–ligand interaction in aqueous media.

The optimized structures are shown in Fig. 7A, confirming that the Br-naphthophen ligand adopts a near-planar

conformation, which minimizes steric hindrance and pre-organizes the N_2O_2 donor cavity for metal uptake. The simulation reveals that the Ag^+ ion preferentially coordinates to the two imine nitrogen atoms, with a calculated bond length of 2.1 Å. The Fe^{3+} ion sits centrally within the N_2O_2 pocket, forming shorter, stronger bonds with the phenolic oxygens (2.0 Å) than the nitrogen donors, consistent with the hard–hard interaction predicted by HSAB theory. The electronic properties and charge-transfer mechanisms were elucidated by analyzing the frontier molecular orbitals (FMOs). In the free ligand, the HOMO electron density is localized primarily on the naphthalene rings and the azomethine linkage, confirming these sites as the electron donors. Upon complexation, the LUMO of the metal–ligand system shifts significantly towards the metal center. The energy difference between HOMO and LUMO serves as a measure of chemical stability.[34] As summarized in Fig. 6B, the ΔE gap decreased, which narrows the band gap and facilitates the ligand-to-metal charge transfer (LMCT), which is directly responsible for the bathochromic shifts observed in the UV-Vis spectra. The molecular electrostatic potential (MEP) surface was generated to visualize the reactive sites, as shown in Fig. 7C. The red-colored regions (negative potential) are concentrated around the imine nitrogen and phenolic oxygen atoms, identifying them as nucleophilic sites prone to electrophilic attack by metal cations.[35] Conversely, the blue regions (positive potential) correspond to the aromatic protons. This electrostatic landscape confirms that the N_2O_2 region is the active trap for positively charged Ag^+ and Fe^{3+} ions.

3.8 Comparative analysis of the performance of BNP@RHNS sensor

The BNP@RHNS sensor was compared to previously reported solid-state spectrophotometric probes for Ag^+ and Fe^{3+} detection, as described in Table 1. For Ag^+ detection, BNP@RHNS has a limit of detection (LOD) of 0.185 ppm which is competitive with several other sensing platforms that have been established: ionophore-based optical probes (LOD = 0.090 ppm), dehydrogenase enzyme electrodes (0.054 ppm), and PICS-type systems (0.190 ppm). Certain highly engineered hybrid nanomaterials like HMAN/CNF composites have lower detection thresholds at 0.007 ppm; however, those platforms require much more complicated multi-step fabrication procedures. BNP@RHNS gets its silica scaffold directly from agricultural rice husk waste by a simple thermochemical sol–gel route without expensive precursors or complicated functionalization chemistry. In the field of sustainable low-cost solid-state sensors, the current 0.185 ppm LOD is practically relevant in terms of detection capability for the monitoring of Ag^+ in environmental and E-waste matrices. For Fe^{3+}, BNP@RHNS has a limit of detection of 0.247 ppm. Several systems are compared in Table 1 that show lower limits of detection, namely the TSQ sensor at 0.056 ppm, CHBAN-CNM at 0.082 ppm, and Phimhb platform at 0.011 ppm; the last one is the most sensitive probe among this comparison set. However, these systems use solution-phase assay formats or need complicated ligand architectures or use carbon nanomaterial scaffolds whose production has a much higher material cost and environmental footprint. The BNP@RHNS sensor uses a structurally simple π-conjugated Schiff base anchored on agro-waste-derived mesoporous silica support and gets a Fe^{3+} LOD better than that of pyrophosphate-AuNPs (0.165 ppm) and benzochromone-based Schiff-base sensors (0.313 ppm). All data in Table 1 indicate that BNP@RHNS fits into a very specific category; it does not pretend to have the lowest absolute detection limits in its class but rather offers an acceptable mix of analytical sensitivity, ease of operation, quick response time, and real material sustainability which together set it apart from both more sensitive but complex platforms as well as simpler yet less capable alternatives.

Table 1 A comparison of BNP@RHNS's analytical performance against other reported solid-state sensors

Target ion	Sensor material	LOD/ppm	Ref.
Ag^+	Ionophore-based sensor	0.090	36
	Dehydrogenase enzyme electrode	0.054	37
	PICS	0.190	38
	HMAN/CNF	0.007	33
	BNP@RHNS	0. 185	This work
Fe^{3+}	TSQ sensor	0.056	39
	CHBAN-CNM	0.082	40
	Pyrophosphate-AuNPs	0.313	41
	Benzochromone-based Schiff base	0.160	42
	Phimhb sensor	0.011	43
	BNP@RHNS	0.247	This work

3.9 Application

3.9.1 Determination of Ag^+ and Fe^{3+} ions in real water samples. The proposed BNP@RHNS sensor's practical feasibility and accuracy for environmental monitoring were validated by using it to quantify Ag^+ and Fe^{3+} in real water. Tap water samples were analyzed. The Standard Addition Method was used to remove matrix interference, acknowledging the potential complexity of the sample matrices. The protocol involved adding known amounts of standard Ag^+ and Fe^{3+} solutions to actual samples and then determining the recovery percentages. Table 2 presents a summary of the analytical results. The sensor demonstrated excellent performance, with recovery values ranging from 97.37% to 100.73% and an RSD of less than 4.0% ($n = 3$). These results indicate that the co-existing organic and inorganic species present in natural waters do not significantly interfere with the sensing mechanism. To confirm the BNP@RHNS sensor's accuracy and reliability for real-world applications, its results were compared to those from the standard ICP-OES method.

3.9.2 Detection of Ag^+ in E-waste. The detection of Ag^+ ions in electronic waste was achieved through a meticulous, staged methodology. In the initial phase, WPCBs were subjected to grinding. The resulting powder was then mixed with a solution comprising 2.0 M H_2SO_4 and 0.2 M H_2O_2, which underwent heating for a sustained period of 6 h at 90 °C. This procedure aimed to diminish potential interference by dissolving and reducing the concentrations of several metals, including Zn, Co,

Table 2 Determination of Ag^{+} and Fe^{3+} using BNP@RHNS sensor

			Proposed method		ICP-OES method	
Samples	Target ion	Added (ppb)	Found[a] (ppb)	Recovery (%)	Found[a] (ppb)	Recovery (%)
Tap water	Ag^{-}	—	ND[b]	—	ND[b]	—
		200	198.17 ± 0.29	99.08	199.00 ± 0.20	99.50
		300	300.60 ± 0.20	100.20	300.07 ± 0.15	100.02
		400	400.60 ± 0.20	100.15	400.23 ± 0.15	100.10
WPCBs		—	248 ± 0.27	—	279 ± 0.15	—
Tap water	Fe^{3+}	—	8.67 ± 0.45	—	8.63 ± 0.21	—
		300	309.73 ± 0.25	100.36	308.73 ± 0.15	100.03
		400	409.77 ± 0.25	100.28	408.93 ± 0.12	100.08
		500	509.63 ± 0.20	100.19	507.80 ± 0.10	99.83

[a] Mean ± standard deviation ($n = 3$). [b] Not detected.

Mn, Li, Fe, Ni, Al, and Cu. Afterward, the leftover material from this stage was treated with a 50% HNO_3 solution. Aqua regia leaching was employed during the third phase to dissolve the Ag^{+} ions in the residual material. At the final stage, 1.0 M NaOH was added to set the solution's pH to 6.2, followed by the detection of Ag^{+} ions *via* the BNP@RHNS sensor, as detailed in Table 2.

To assess the potential interference of ionic by-products generated during the acid digestion and neutralization steps (principally Na_2SO_4 and $NaNO_3$), a control experiment was conducted in which the BNP@RHNS sensor was exposed to a solution of equivalent ionic strength (adjusted using $NaNO_3$) in the absence of any target metal ions. The resulting UV-Vis absorbance at $\lambda_{max} = 250$ nm was statistically indistinguishable from that of the buffer blank ($p > 0.05$, $n = 3$), confirming that residual background salts at the concentration levels present in the working leachate solution do not measurably perturb the absorbance baseline or the sensing equilibrium.

4 Conclusions

In this work, a new dual-functional nanocomposite sensor, BNP@RHNS, was successfully engineered *via* a facile and sustainable route, valorizing agricultural waste (rice husk) into a high-value sensing platform. The successful immobilization of the ligand onto the nanosilica framework was structurally confirmed by FTIR, XRD, and FE-SEM analyzes, which revealed a preserved porous architecture with high surface accessibility. The sensor developed showed outstanding analytical capabilities for sequentially detecting Ag^{+} and Fe^{3+} ions in water using spectrophotometry. Under optimized conditions (pH 6.2 for Ag, pH 3.6 for Fe), the sensor exhibited a rapid response time of less than 40 s and obeyed Beer's law with wide linear dynamic ranges. LOD values were calculated to be 0.185 ppm and 0.247 ppm. These values are close to the recommended safety limits set by the World Health Organization (WHO) for Ag^{+} in drinking water, demonstrating the practical feasibility of the sensor for monitoring environmental and E-waste matrices. Ultimately, this study presents the BNP@RHNS sensor as a robust tool for environmental monitoring and a prime example of the waste-to-wealth paradigm. Experimental spectral shifts were corroborated by density functional theory (DFT) calculations, which confirmed the thermodynamic spontaneity of the complexation and identified the N_2O_2 cavity and the azomethine/phenolic sites as the key centers for chelation and charge transfer (LMCT). Furthermore, the sensor displayed excellent chemical stability and reusability for up to 6 cycles and was successfully applied to the determination of metal ions in real tap water samples, achieving high recovery rates of 97.37% to 100.73%. Crucially, the sensor exhibited excellent chemical stability, reusability, and robust interference tolerance. It was successfully applied not only to the determination of metal ions in environmental water matrices but also to the recovery analysis of Ag^{+} in complex E-waste leachates. Future research will prioritize expanding this application to more chemically complex environments, such as river water and untreated industrial effluents, to rigorously evaluate the sensor's robustness against higher organic and inorganic loading. Ultimately, this study presents the BNP@RHNS sensor not only as a robust tool for environmental monitoring but also as a prime example of the waste-to-wealth paradigm, bridging the gap between green materials science and advanced analytical chemistry.

Conflicts of interest

There are no conflicts to declare.

Data availability

The data that support the findings of this study are available from the corresponding author upon reasonable request.

Supplementary information (SI) is available. See DOI: https://doi.org/10.1039/d6ra02312f.

Acknowledgements

This Project was funded by the Deanship of Scientific Research (DSR) at King Abdulaziz University, Jeddah, Saudi Arabia under grant no. (GPIP: 1287-662-2025). The authors, therefore, acknowledge with thanks DSR for technical and financial support.

References

1 E. J. Mitchell and S. H. Frisbie, *PLoS One*, 2023, **18**, e0287937.
2 Y. Jurczynski, R. Passos and L. C. Campos, *Sustainability*, 2024, **16**, 7107.
3 H. M. Abumelha, N. M. Alourfi, A. S. Al Zbedy, A. Alharbi, N. Alkhathami, I. Mousa, M. A. Khalil and N. M. El-Metwaly, *J. Water Proc. Eng.*, 2025, **77**, 108381.
4 A. Sarker, J.-E. Kim, A. R. M. T. Islam, M. Bilal, M. R. J. Rakib, R. Nandi, M. M. Rahman and T. Islam, *Environ. Sci. Pollut. Res.*, 2022, **29**, 3230–3245.
5 H. M. Saleh, A. I. Hassan and R. N. Khalef, in *Environmental Impact and Remediation of Heavy Metals*, ed. H. M. Saleh and A. I. Hassan, IntechOpen, London, 2022, DOI: 10.5772/intechopen.103907.
6 M. Dettori, A. Arghittu, G. Deiana, P. Castiglia and A. Azara, *Environ. Res.*, 2022, **209**, 112773.
7 A. Bhat, K. Ravi, F. Tian and B. Singh, *Pollutants*, 2024, **4**, 196–211.
8 J. Auclair and F. Gagné, *Nanomaterials*, 2022, **12**, 3107.
9 Z. Mat Lazim, S. Salmiati, M. Marpongahtun, N. Z. Arman, M. R. Mohd Haniffah, S. Azman, E. L. Yong and M. R. Salim, Water, 2023, **15**, p. 1349.
10 M. Muhaidin, F. H. Naning, J. M. Saad, R. Wahi and T. Zangina, *J. Adv. Res. Micro Nano Eng.*, 2024, **18**, 78–102.
11 J. Doroszkiewicz, J. A. Farhan, J. Mroczko, I. Winkel, M. Perkowski and B. Mroczko, *Int. J. Mol. Sci.*, 2023, **24**, 15721.
12 S. Levi, M. Ripamonti, A. S. Moro and A. Cozzi, *Mol. Psychiatr.*, 2024, **29**, 1139–1152.
13 I. Ziani, H. Bouakline, A. El Guerraf, A. El Bachiri, F. Marie-Laure and F. Sher, *Trends Food Sci. Technol.*, 2025, **156**, 104850.
14 D. Cozzolino and J. Chapman, *Anal. Bioanal. Chem.*, 2024, **416**, 611–620.
15 K. B. Beć, J. Grabska and C. W. Huck, *Foods*, 2022, **11**, 1465.
16 A. Li, C. Yao, J. Xia, H. Wang, Q. Cheng, R. Penty, Y. Fainman and S. Pan, *Light: Sci. Appl.*, 2022, **11**, 174.
17 M. P. Kabiraz, P. R. Majumdar, M. C. Mahmud, S. Bhowmik and A. Ali, *Heliyon*, 2023, **9**, 4.
18 D. Dorairaj, N. Govender, S. Zakaria and R. Wickneswari, *Sci. Rep.*, 2022, **12**, 20162.
19 R. M. A. Rahman, M. P. Paraman, S. R. Christopher, K. Pandian, R. V. Solomon, S. K. Sevathapandian, G. Arumugam and K. Karunanandham, *Biomass Convers. Biorefinery*, 2024, 1–16.
20 M. S. C. Ibrahim, T. H. Meng, A. Ahmad, M. S. M. Ghazali, W. R. W. Abdullah and N. L. Chuen, *Adv. Nat. Sci. Nanosci. Nanotechnol.*, 2022, **13**, 033001.
21 A. D. Salman, T. Juzsakova, P.-C. Le, M. G. Jalhoom, T. A. Abdullah, E. Domokos, H.-S. Le, S. W. Chang, S. C. Kim and D. D. Nguyen, *Biomass Convers. Biorefinery*, 2023, **13**, 9411–9421.
22 B. A. Salami, T. A. Oyehan, Y. Gambo, S. O. Badmus, G. Tanimu, S. Adamu, S. A. Lateef and T. A. Saleh, *Environ. Sci. Pollut. Res.*, 2022, **29**, 42560–42600.
23 X. Xu, S. Yang, Y. Wang and K. Qian, *Green Anal. Chem.*, 2022, **2**, 100020.
24 W. Mazi, O. Alaysuy, K. M. Alkhamis, M. A. Alsharif, A. S. A. Zbedy, R. Almughathawi, B. A. Babgi and N. M. El-Metwaly, *J. Mol. Struct.*, 2026, **1351**, 144294.
25 T. B. Benzaquén, P. M. Carraro, G. A. Eimer, J. Urzúa-Ahumada, P. S. Poon and J. Matos, *Molecules*, 2025, **30**, 2484.
26 S. H. Ali, M. Y. Emran and H. Gomaa, in *Waste Recycling Technologies for Nanomaterials Manufacturing*, Springer, 2021, pp. 541–588.
27 I. J. Fernandes, D. Calheiro, F. A. Sánchez, A. L. D. Camacho, T. L. A. C. Rocha, C. A. M. Moraes and V. C. d. Sousa, *Mater. Res.*, 2017, **20**, 512–518.
28 W. Guo, G. Li, Y. Zheng and K. Li, *RSC Adv.*, 2021, **11**, 34915–34922.
29 M. Bandyopadhyay, U. Sengupta, M. Periyasamy, S. Mukhopadhyay, A. Hasija, D. Chopra, N. Özdemir, M. A. Said and M. K. Bera, *Russ. J. Inorg. Chem.*, 2022, **67**, S114–S127.
30 R. Malav and S. Ray, *RSC Adv.*, 2025, **15**, 22889–22914.
31 N. Y. Elamin, M. R. Elamin, S. Abdalla, M. A. Khalil, A. A. Helaly, B. A. Babgi and M. A. Hussien, *Int. J. Biol. Macromol.*, 2025, **328**.
32 N. Y. Elamin, M. R. Elamin, B. Y. Abdulkhair, A. Subaihi, M. A. Khalil and A. Shahat, *Microchem. J.*, 2025, 213.
33 W. Abd El-Fattah, A. Guesmi, N. Ben Hamadi, M. A. Khalil, A. A. Helaly, B. A. Babgi and M. A. Hussien, *Microchem. J.*, 2025, 218.
34 S. Goswami, K. Aich, S. Das, C. D. Mukhopadhyay, D. Sarkar and T. K. Mondal, *Dalton Trans.*, 2015, **44**, 5763–5770.
35 H. Hadi, G. Bouzid, S. Nasr, H. Ghalla, R. B. Chaabane and S. Ayachi, *Heliyon*, 2023, **9**.
36 A. R. Firooz, A. A. Ensafi, N. Kazemifard and R. Khalifeh, *Sens. Actuators, B*, 2013, **176**, 598–604.
37 Q. Liu and J. R. Kirchhoff, *J. Electroanal. Chem.*, 2007, **601**, 125–131.
38 S. A. Chounechenan, A. Mohammadi and B. Khalili, *Anal. Methods*, 2022, **14**, 3405–3415.
39 X. Liu, N. Li, M.-M. Xu, J. Wang, C. Jiang, G. Song and Y. Wang, *RSC Adv.*, 2018, **8**, 34860–34866.
40 E. Aljuhani, A. S. A. Zbedy, S. A. Alqarni, S. O. Alzahrani, A. Arwa, A. A. Alfi, A. M. A. Bonayan and A. Shahat, *Int. J. Environ. Anal. Chem.*, 2025, **105**(20), 9104–9120.
41 S.-P. Wu, Y.-P. Chen and Y.-M. Sung, *Analyst*, 2011, **136**, 1887–1891.
42 S. A. Alahmady, N. Syed, A. Q. Alorabi and A. A. Elhenawy, *Environ. Technol.*, 2024, **45**, 1542–1556.
43 S. D. Al-Qahtani, R. Shah, E. Aljuhani, Z. A. Al-Ahmed, T. M. Habeebullah, F. Saad, A. Shahat and N. M. El-Metwaly, *ChemistrySelect*, 2022, **7**, e202103402.